# Electrolysis on a chip with tunable thin film nanostructured PGM electrocatalysts generated from self-assembled block copolymer templates

*Deepra Bhattacharya[a], Subarna Kole[a], Orhan Kizilkaya[b], Joseph Strzalka[c], Polyxeni P. Angelopoulou[d], Georgios Sakellariou[d], Dongmei Cao[e], and Christopher G. Arges[a*]*

Deepra Bhattacharya, Subarna Kole, Prof Christopher Arges
Cain Department of Chemical Engineering, Louisiana State University, Baton Rouge, LA 70803
E-mail: carges@lsu.edu

Dr Orhan Kizilkaya
Center for Advanced Microstructures and Devices, Louisiana State University, Baton Rouge, LA 70806

Dr Joseph Strzalka
X-ray Science Division, Argonne National Laboratory, Lemont, IL 60439

Polyxeni P. Angelopoulou, Prof. Georgios Sakellariou
Department of Chemistry, National and Kapodistrian University of Athens, 15771 Athens, Greece

Dr Dongmei Cao
Shared Instrumentation Facility, Louisiana State University, Baton Rouge, LA 70803

*corresponding author: carges@lsu.edu
Keywords: block copolymers; platinum group metals; electrocatalyst; hydrogen pump; water electrolysis

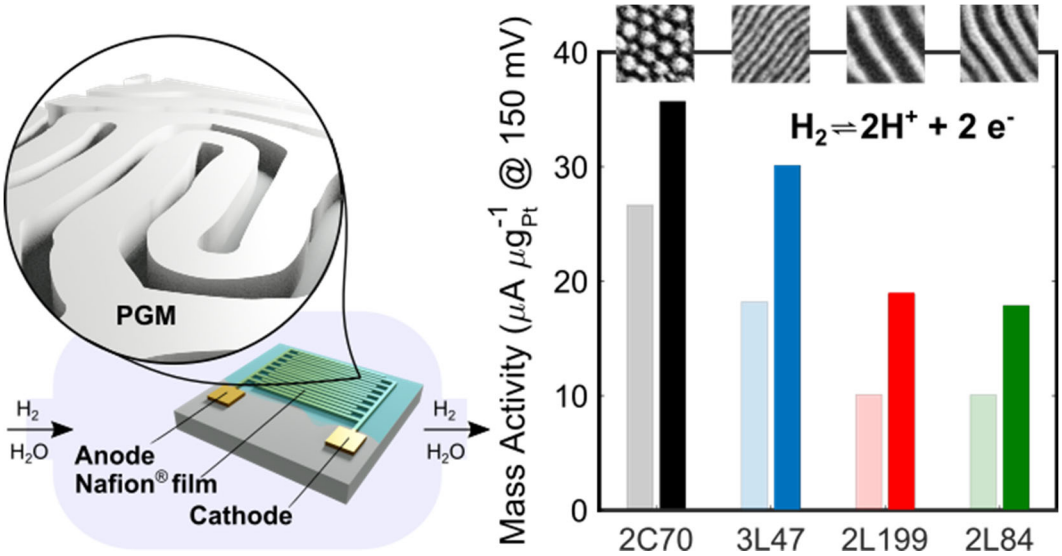


Nanostructured platinum group metal thin films templated from self-assembled block copolymers of tuneable feature size and morphology were tested for electrochemical hydrogen oxidation / hydrogen evolution and water-splitting activity on an interdigitated electrode-based lab-on-a-chip platform.

Self-assembled block copolymers are promising templates for fabricating thin film materials with tuned periodic feature sizes and geometry at the nanoscale. Here, we report a series of nanostructured platinum and iridium oxide electrocatalysts templated from poly(styrene-*block*-poly(vinyl pyridine) (PS*b*PVP) block copolymers via an incipient wetness impregnation (IWI) pathway. Both nanowire and nanocylinder electrocatalysts of varying feature sizes were assessed and higher catalyst loadings have been achieved by the alkylation of the pyridine moieties in the PVP block prior to IWI. Electrocatalyst evaluations featuring hydrogen pump and water electrolysis demonstrations have been carried out on interdigitated electrode (IDE) chips flexible with liquid supporting electrolytes and thin film polymer electrolytes. Notably, the mass activities of the nanostructured electrocatalysts from alkylated block copolymer templates are 35% to 94% higher than electrocatalysts from non-alkylated block copolymer templates. Standing cylinder nanostructures lead to higher mass activities than lamellar variants despite their not having the largest surface area per unit catalyst loading demonstrating that mesostructure architectures have a profound impact on reactivity. Overall, IDE chips with model thin film electrocatalysts prepared from self-assembled block copolymers offer a high-throughput experimental method for correlating electrocatalyst nanostructure and composition to electrochemical reactivity.

## 1. Introduction

Due to their excellent reactivity for catalyzing a variety of electrochemical reactions and their stability at extreme pH values, platinum group metals (PGMs) continue to be the standard-bearer electrocatalysts for fuel cells and water electrolyzers[1-3]. However, proliferation of electrochemical technologies utilizing PGMs is constrained by their high costs[4]. Satisfying the tradeoff between cost and performance necessitates good utilization of PGM electrocatalysts when deployed in electrodes – primarily through the formation of nanostructured architectures[5]. Numerous schemes[1, 3] are available for the preparation of nanoscale PGM electrocatalysts (e.g., liquid colloidal syntheses[6], electrodeposition[7], incipient wetness impregnation[8], and physical vapor deposition[9]). The rich

library of methods for preparing nanostructured PGMs with diverse heterogeneity has resulted in electrocatalysts with extremely high surface areas and catalytic activity. Fine-structure PGM electrocatalysts with atomic-scale precision have been prepared (e.g., single crystals[10]), but the systematic engineering of PGM catalyst nanostructure over large (several $mm^2$) areas is less ubiquitous.

Directed self-assembly of block copolymers (BCPs) is a bottom-up nanomanufacturing platform that realizes dense, periodic nanoscale structures with simple architectures and long-range order[11-13]. Such nanostructures can be systematically tuned to obtain various morphologies and periodic feature sizes (3 to 50 nm)[11, 14, 15]. For instance, varying the volume fraction ($f$) of one polymer block in relation to its other block for A-B canonical diblocks and A-B-A triblocks can systematically generate lamellar, gyroid, cylindrical, and spherical morphologies[16, 17]. The overall degree of polymerization ($N$) of the BCP dictates the periodic spacing ($L_0$) of the microphase separated material (e.g., $L_0 \sim \chi^{1/6}N^{2/3}$ for BCPs in the strong-segregation limit)[14, 17].

There are two main strategies for generating metallic nanostructures from self-assembled BCP templates. The first of these involves physical vapor deposition (PVD) or chemical vapor deposition (CVD) of metals[18-25] on the BCP template, usually before and/or after the removal of one or more blocks by plasma treatment or chemical dissolution/lift-off. For example, Ross and co-workers[24, 26] fabricated metallic nanowires of varying compositions (e.g., Ti, W, Pt, Co, and Au) from poly(styrene-*block*-dimethylsiloxane) (PS*b*PDMS) parallel cylinders via a combination of PVD and plasma treatment with $O_2$ and $CF_4$. The second method involves incipient wetness impregnation (IWI)[6, 8, 27-34] followed by reduction of metals and removal of the BCP template[35, 36]. An example of IWI by Buriak and co-workers[8] selectively infiltrated precious metal precursors (e.g., acid or salt forms of chloroplatinate, chloropalladate, chloroaurate) into the polar domains of self-assembled poly(styrene-*block*-2-vinyl pyridine) (PS*b*P2VP) followed by $O_2$ and Ar plasma treatment to remove the polymer template and reduce the metals to yield Pt, Pd, and Au nanowires on silicon wafers. Additionally, PGM

metallic structures from BCPs have also been produced from self-assembled micelles[6, 37] or other self-assembled structures in bulk solution[28, 29, 38] as opposed to templating with self-assembled thin films.

There are several existing reports of periodic PGM structures from self-assembled BCP templates that demonstrate electrochemical activity. Most of these reports rely on micellar deposition of self-assembled BCPs limiting the types of nanoscale geometries that can be investigated. St-Pierre and co-workers[6] demonstrated methanol oxidation from Pt nanoparticles on glassy carbon through deposition of (poly(styrene-*block*-4-vinyl pyridine) (PS*b*P4VP) micelles and IWI. Yan and co-workers[37] prepared multiple layers of Pt nanoparticles on carbon paper as a cathode (loading of 0.05 $mg_{Pt}$ $cm^{-2}$) using self-assembled PS*b*P4VP micelles and IWI. They obtained a power density of 0.4 W $cm^{-2}$ with hydrogen and oxygen at 80 °C/100% RH for a low-temperature proton exchange membrane fuel cell (LT-PEMFC). Rider and co-workers[28] reported formic acid oxidation with bimetallic Pt-Ir electrocatalysts of varying stoichiometries from self-assembled PS*b*P4VP micelles and IWI. They also prepared bimetallic Pt-Au nanostructures[27] using a similar procedure for electrochemical methanol oxidation. Kim and co-workers[33] fabricated Pt nanomeshes from several layers of self-assembled PS*b*P2VP thin films using IWI. The nanomesh layers consisted of stacked perpendicular and parallel cylinder structures. These structures were characterized for the hydrogen evolution reaction (HER) with aqueous sulfuric acid electrolyte. Notably, the nanomeshes were less active for HER when compared to commercial Pt nanoparticles on high surface area carbon supports. In another report[31], Kim and co-workers prepared Pt, Pd, Au, and Co nanoparticles from PS*b*P4VP on samarium-doped ceria (SDC) electrodes for the hydrogen oxidation reaction (HOR) in solid oxide fuel cells (SOFCs). The nanoparticles were coated with SDC after preparation to prevent coalescence at 600 °C. Pt-SDC yielded the best HOR performance. Finally, Ho and co-workers[29] prepared nanoporous Pt meshes from gyroid forming poly(styrene-*block*-lactate) (PS*b*PLA) for methanol oxidation. This procedure performed acid hydrolysis of the PLA domain followed by impregnation with chloroplatinic acid and chemical reduction with hydrazinium hydroxide. The polystyrene microdomain was removed through

UV degradation. In summary, BCP templated PGM nanostructures have been developed via several fabrication pathways, and their electrochemical activity has been investigated in multiple experimental platforms for various electrocatalytic reactions. However, none of these reports include a systematic investigation of how catalyst morphology and periodic feature size impact electrochemical activity.

In this work, different nanoscale geometries of Pt electrocatalysts prepared from self-assembled BCP templates were correlated with electrochemical HER/HOR activity in a hydrogen pump setup on interdigitated electrode (IDE) lab-on-a-chip platforms with a thin film of Nafion® as a polymer electrolyte. IDE chips were selected for electrochemical reactivity assessments because of their inherent compatibility with the BCP templating process. Moreover, water electrolysis (HER/OER) experiments were also performed on the IDE lab-on-a-chip platform demonstrating the versatility of the platform for use with various electrocatalyst materials (Pt, $IrO_x$) and current collectors (Au, Pt) as well as both liquid (0.1 M perchloric acid) and solid (Nafion® thin film) electrolytes. Overall, the IDE lab-on-a-chip platform is envisioned as an effective high-throughput tool for screening electrocatalyst composition and nanostructure, as well as electrolyte type, and their role on electrochemical activity. The BCPs used for the templating process are listed in **Table 1**. The templating process for fabricating nanostructured electrocatalysts from PS*b*P2VP is illustrated in **Figure 1**. The procedure involving PS*b*P4VP, which is slightly different, is conveyed in **Figure S1**. It is to be noted that two different variants of metal nanostructures were developed from each BCP template: the first pathway involves pattern transfer by direct IWI of the self-assembled PS*b*PVP template (path 2 in **Figure 1**), while the second pathway involves alkylating the BCP template to yield N-methyl pyridinium (PS*b*PVP/$NMP^+$) through a Menshutkin reaction[39] (path 1a–b in **Figure 1**). This latter pathway involving PS*b*PVP/$NMP^+$ is previously unreported and leads to larger metal loadings and taller mesoscale structures over the former, conventional pathway involving PS*b*PVP.[8, 30-33] The terms PS*b*PVP/$NMP^+$ and PS*b*PVP refer to alkylated and non-alkylated BCP variants with either 2-vinylpyridine and 4-vinylpyridine repeat units and A-B diblock and A-B-A triblock configurations.

**Table 1.** Identification labels, properties, and morphology of BCP templates utilized

| Template ID | Polymer Name | Mn (g mol$^{-1}$) | $w_{PS}$ | Morphology[a] | Domain Spacing $L_0$ (nm) [b] | Film Thickness (nm) |
|---|---|---|---|---|---|---|
| **2L84** | PS*b*P2VP | 84,000 | 0.47 | Lamellar | 44.59±0.63 | 43.87 |
| **2L199** | PS*b*P2VP | 199,000 | 0.51 | Lamellar | 68.54±0.72 | 81.68 |
| **3L47** | P2VP*b*PS*b*P2VP | 47,000 | 0.48 | Lamellar | 22.37±0.18 | 35.41 |
| **2C70** | PS*b*P4VP | 69700 | 0.69 | Cylindrical | 49.81±0.31 | 46.50 |

[a] All self-assembled structures were oriented perpendicular to the IDE surface
[b] calculated from GISAXS measurements; uncertainties indicate standard errors of the mean

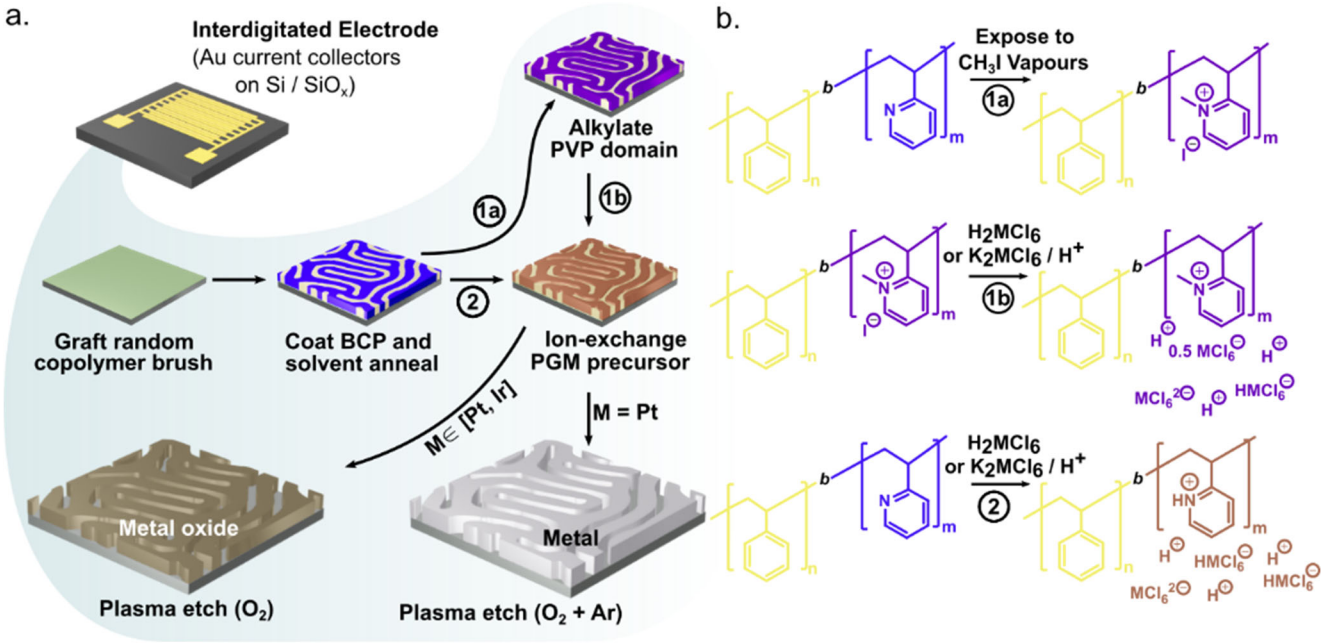


**Figure 1.** a.) Fabrication procedure of metal nanostructures from self-assembled BCP templates with perpendicular lamellae morphology. b.) Two types of BCP template chemistries were evaluated: PS*b*PVP/NMP$^+$ (pathway 1) and PS*b*PVP (pathway 2)

SEM images of all self-assembled block copolymers (BCPs) used in this study along with the Pt nanostructures attained from them are in **Figure 2**. Only the alkylated BCPs were imaged since the N-methyl pyridinium iodide in PS*b*PVP/NMP$^+$ provides greater contrast for SEM imaging and it has previously been demonstrated that exposure to iodomethane vapor does not alter the self-assembled morphology[39]. The electron micrographs in **Figures 2a-c**, corresponding to templates 2L84, 2L199,

and 3L47, convey that perpendicular lamellae of various periodic feature sizes were attained by adjusting the overall $M_n$ of the PS*b*P2VP based templates. The PS*b*P4VP based template (2C70) yielded perpendicular cylinders (**Figure 2d**).

**Figures 2e – h** show Pt nanostructures from PS*b*PVP templates, while **Figures 2i – l** convey Pt nanostructures templated by the PS*b*PVP/$NMP^+$. SEM images of the metallic nanostructures over larger areas (e.g., 5 μm × 5μm) with insets of two-dimensional Fast Fourier Transform (FFT) patterns are provided in **Figure S2**. **Figure S2g** presents the $IrO_x$ nanostructures from the alkylated 3L47 template. From the images and the multiple halos observed in the FFT insets, it is evident that the

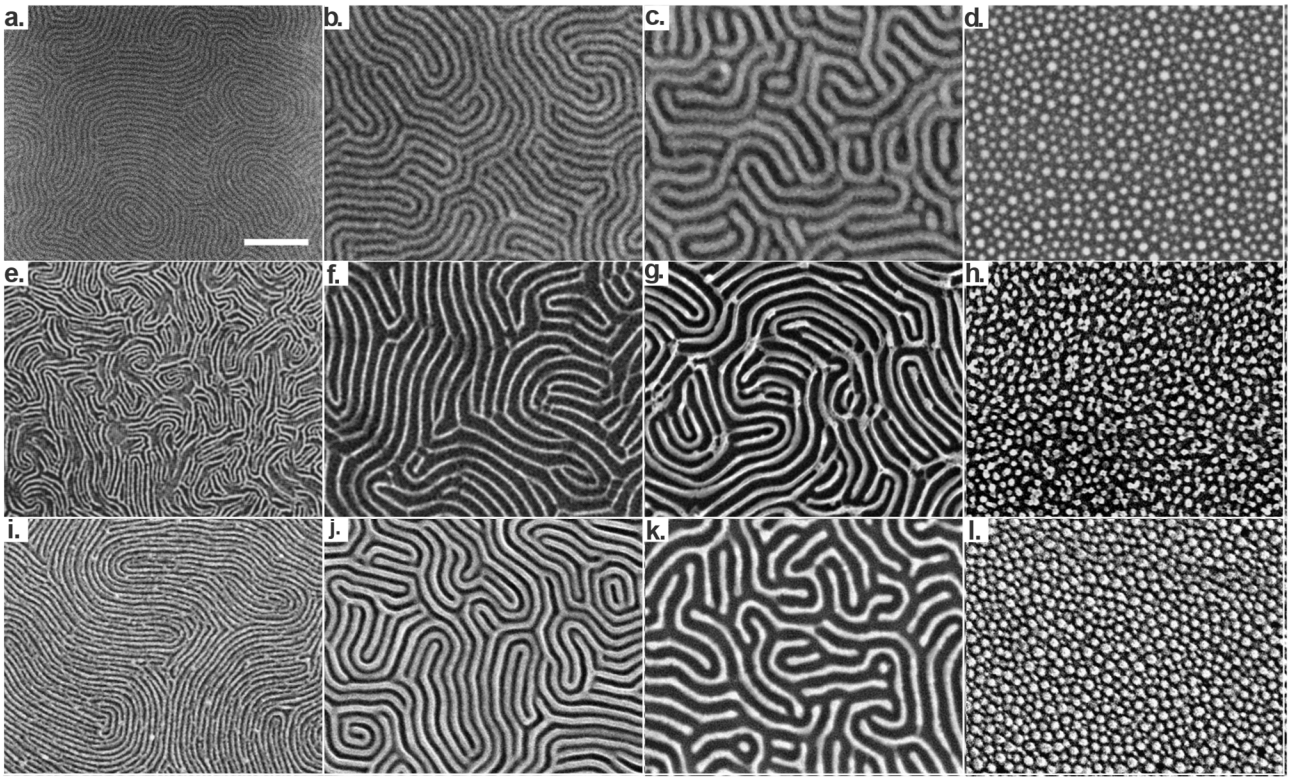


**Figure 2.** SEM images of (a–d) PS*b*PVP/$NMP^+$, (e–h) Pt nanostructures from self-assembled PS*b*PVP templates (i.e., non-alkylated template), (i–l) Pt nanostructures from self-assembled PS*b*PVP/$NMP^+$ templates (i.e., alkylated template). Columns 1 – 4 depict images from 3L47, 2L84 2L199, and 2C70, block copolymers/nanostructures from block copolymer templates, respectively. Scale bar at (a) denotes 250 nm and applies to all images.

metallic nanostructures retained the long-range order of the BCPs from which they were templated. The nanostructure and morphology of each BCP remained intact throughout the fabrication process to

produce metal nanostructures of varying periodicity and spacing. It may further be noted that the alkylated variants of the BCP templates showed thicker lateral features than the non-alkylated variants.

**Table 2.** PGM loadings per geometric area, average thicknesses of thin film electrocatalyst structures, and the estimated surface areas of the PGM catalysts per unit geometric area and PGM mass loading

| Sample ID[a] | Mass loading of PGM ($\mu g_{PGM}$ $cm^{-2}_{geo}$) [b] | Average topographical height value (nm) [b] | Surface area of PGM per unit geometric area ($cm^2_{PGM}$ $cm^{-2}_{geo}$) [b] | Surface area of PGM per unit mass ($cm^2_{PGM}$ $\mu g_{PGM}^{-1}$) |
|---|---|---|---|---|
| **2L84-Pt** | 4.95±0.16 | 11.9±0.40 | 0.94±0.013 | 0.19 |
| **2L84-A-Pt** | 9.68±0.14 | 28.0±0.34 | 1.91±0.028 | 0.20 |
| **2L199-Pt** | 5.85±0.19 | 34.1±0.19 | 1.53±0.041 | 0.27 |
| **2L199-A-Pt** | 11.25±0.03 | 56.6±0.12 | 2.55±0.003 | 0.23 |
| **3L47-Pt** | 1.58±0.12 | 8.5±0.32 | 0.85±0.044 | 0.54 |
| **3L47-A-Pt** | 3.83±0.23 | 17.4±0.14 | 2.27±0.056 | 0.59 |
| **3L47-A-$IrO_x$** | 2.67 (Ir) ±0.14 | 17.7±0.21 | 2.31±0.013 | 0.87 |
| **2C70-Pt** | 3.60±0.13 | 13.3±0.62 | 1.09±0.020 | 0.30 |
| **2C70-A-Pt** | 11.72±0.12 | 22.3±0.56 | 2.34±0.038 | 0.20 |

[a] alkylated ($PSbPVP/NMP^+$) templates are designated by the letter 'A' after the template ID.
[b] experimental uncertainties indicate standard errors of the mean

AFM imaging was carried out to determine thicknesses of the metal nanostructures. **Figure S3** provides the AFM topography images of Pt nanostructures templated from PS*b*PVP and $PSbPVP/NMP^+$. The average heights of the Pt structures determined from the images are reported in **Table 2**. This table also provides the Pt and Ir loadings determined from ICP–OES experiments, (data corresponding to which are available in **Figure S4**) and the calculated surface area values of the metal nanostructures per geometric area and PGM loading (computed by combining the lateral surface area

from SEM images with the height data from AFM images). The surface area calculation procedure is exemplified in **Figure S5a**.

Substantiating the thicker lateral feature sizes observed in the SEM images (**Figure 2**), the AFM heightmaps and PGM loading results demonstrate that the PVP/$NMP^+$ templates lead to nanostructures of increased out-of-plane thickness as well as higher PGM loadings. This enhanced robustness of the metal nanostructures obtained from alkylated BCP templates is ascribed to the fact that the alkylated PVP/$NMP^+$ domain, being more hydrophilic than the non-alkylated PVP domain due to the presence of fixed charge carriers, experiences greater swelling in the precursor solution and allows for a greater uptake of the PGM salt.

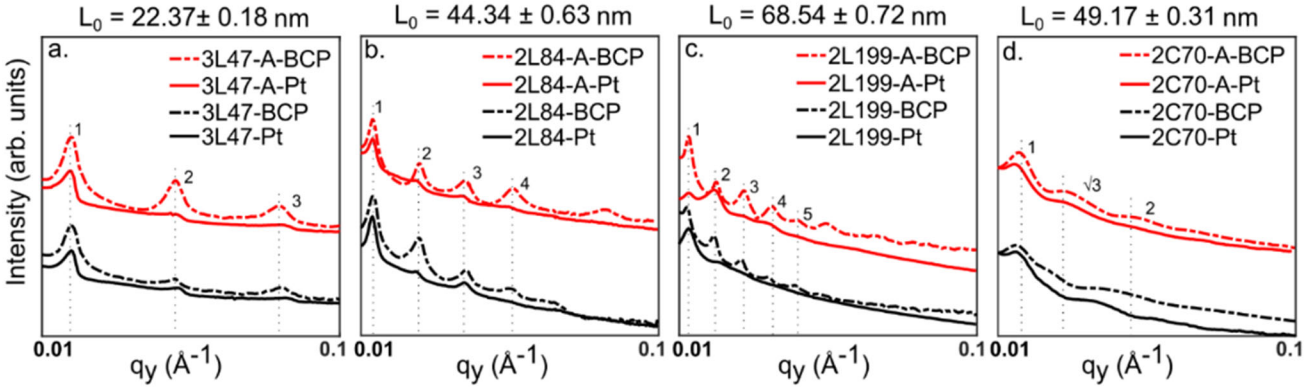


**Figure 3.** One dimensional GISAXS profiles along the in-plane scattering vector for Pt nanostructures and their corresponding templates of alkylated and non-alkylated (a) 3L47 (b) 2L84 (c) 2L199 (d) 2C70.

Nanostructures with a high degree of uniformity are important for drawing definitive conclusions between feature sizes and/or morphology and electrochemical activity. Because the electron and AFM micrographs only provide a local assessment of the microstructures, GISAXS was deployed to assess the structures over larger areas. **Figure S6** provides the 2D GISAXS patterns from all BCP templates and metal nanostructures generated from them, while **Figure 3** consolidates and presents the corresponding one-dimensional profiles obtained along the in-plane scattering vector**.** It is to be noted that the sample identifications in **Figure 3** and **Figure S6** adopt the nomenclature from

**Table 2**, with the block copolymer templates designated by 'BCP' and alkylated variants designated by 'A'.

In **Figures 3a – c**, scattering profiles corresponding to the lamellae forming PS*b*P2VP and PS*b*P2VP/NMP$^+$ templates show 3 to 5 Bragg diffraction peaks, indicating excellent ordering of the self-assembled BCP domains. Additionally, it can be seen that alkylated and non-alkylated templates have the same peak positions for any given BCP, substantiating that the self-assembled nanostructure remains intact after exposure to iodomethane and the formation of N-methyl pyridinium iodide moieties. Profiles obtained from PS*b*P2VP/NMP$^+$ templates show higher intensities because of the change in the electron density of the P2VP domain relative to the PS domain due to the introduction of the iodide groups. **Figure 3a – c** also presents the 1D scattering profiles of the metal nanostructures generated from the lamellae forming BCP templates. The superimposed spectra qualitatively demonstrate that there are no discernable changes in peak positions between each template and its corresponding nanostructure. In addition, peak positions and $q$-spacings were obtained from gaussian fits of the 1-D profiles in **Figure 3a – c**, and domain spacings ($L_0$) of the nanostructures were calculated. The $L_0$ values corresponding to each BCP template (specified above each subplot) remain unchanged through the templating process to metallic structures (with relative error consistently < 5%) signaling that the BCP pattern was transferred to the metal nanostructures with near perfection. There is the notable appearance of a halo observed in the 2D GISAXS patterns of the nanostructured metal in **Figure S6** because of the multiple x-ray scattering events that take place in the extended surfaces of the metallic thin films.

**Figure 3d** shows the 1D GISAXS profiles corresponding to the cylinder forming 2C70 template. Alkylated and non-alkylated BCP templates have the same first-order peak position, as do the metal nanostructures attained from them, indicating that the pattern transfer process succeeded for the

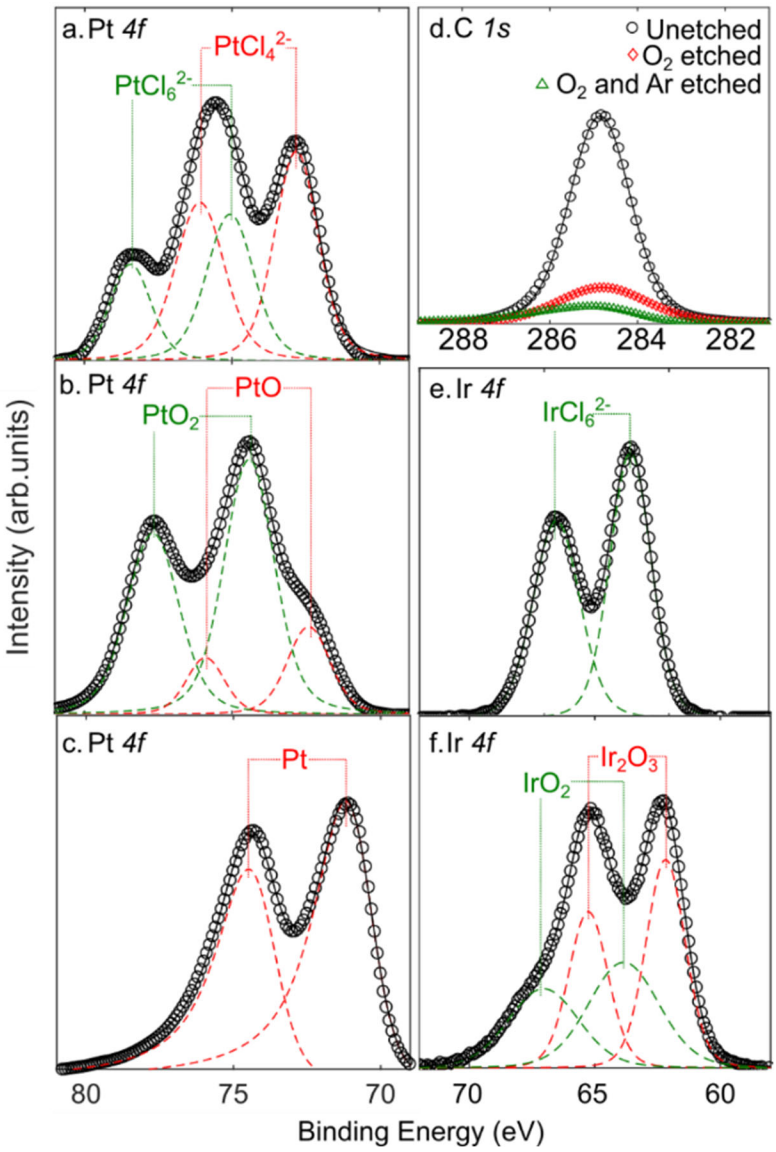


**Figure 4.** XPS Pt *4f* spectra of (a) BCP thin film after ion-exchange with hexachloroplatinate, (b) Pt oxide after oxygen plasma treatment, and (c) metallic Pt after argon plasma treatment. (d) C *1s* spectra of the samples during various fabrication steps (e) Ir *4f* spectra for BCP thin films ion-exchanged with hexachloroiridate, and (f) resulting $IrO_x$ materials after oxygen plasma treatment. Circles indicate raw XPS spectra, while fitted spectra are represented by solid lines, and component peaks are indicated by dashed lines.

2C70 template. The presence of a first-order peak also indicates the presence of nanostructures. However, higher-order peaks for each profile appear significantly broadened, indicating amorphous packing as opposed to the hexagonal closed packing (hcp) expected of perpendicular cylinders. Hence, GISAXS substantiates the morphology observed in the SEM images in **Figure 2** and **Figure S2**. The lack of hexagonal packing may have occurred due to preferential wetting of the of the 2C70 template

on the substrate surface, or due to imperfect annealing with tetrahydrofuran. However, because it is evident from GISAXS that pattern transfer with the cylindrical BCP nanostructure succeeded, electrocatalysts fabricated using the 2C70 template were considered suitable candidates for the present work since they are of a significantly and quantifiably distinct morphology and the focus of the present work is on assessing the effect of varying mesoscale morphology on catalytic activity.

The chemical transformation of the samples from BCP thin films infiltrated with metal precursors ($[MCl_6]^{2-}$) to the metal/metal oxide nanostructures was confirmed by XPS. **Figure 4a** presents the high-resolution Pt 4*f* spectrum corresponding to a BCP film after IWI. The fitted spectrum reveals two pairs of split peaks for $[PtCl_6]^{2-}$ (Pt $4f_{7/2}$: 75.05 eV, Pt $4f_{5/2}$: 78.35 eV, splitting: 3.3 eV), and $[PtCl_4]^{2-}$ (Pt $4f_{7/2}$: 72.8 eV, splitting: 3.27 eV) confirming the infiltration of chloroplatinate into the BCP thin film. The presence of $[PtCl_4]^{2-}$, while unexpected, does not interfere with the process to incorporate Pt salt precursors to generate mesoscale Pt structures, since both chloroplatinate varieties get oxidized to $PtO_x$ and subsequently reduced to elemental Pt. **Figure 4b** shows the high-resolution Pt *4f* spectrum taken after treatment of the Pt-infiltrated BCP film with oxygen plasma. Similar to **Figure 4a**, the fitted spectrum reveals a pair of split peaks, but with a prominent shift towards lower binding energies corresponding to the oxidation of the chloroplatinate to $Pt^{(II)}$ (Pt $4f_{7/2}$: 72.85, splitting: 3.47 eV) and $Pt^{(IV)}$ (Pt $4f_{7/2}$: 74.9, splitting: 3.41 eV) oxides. Further evidence of the reduction of chloroplatinate is observable in the substantial depletion of the Cl *2p* (198.65 eV) peak in XPS survey scan after oxygen plasma treatment (**Figure S7a**). The fitted Pt *4f* spectrum of the BCP film after oxygen and argon plasma treatment (**Figure 4c**) shows a single pair of split peaks confirming the reduction of the Pt oxides observed in **Figure 4b** to elemental $Pt^{(0)}$ (Pt $4f_{7/2}$: 71.0 eV, splitting: 3.3 eV). Evidence of removal of the BCP template during plasma treatment is in the C *1s* (284.8 eV) spectra given in **Figure 4d**, where successive etching steps are observed to lead to decreases in background-normalized peak

intensity. Additional confirmation of the removal of the BCP template is substantiated by the emergence of Si *2s* (153.65 eV) and *2p* (99.4 eV) peaks in the XPS survey spectra taken after plasma treatment (**Figure S7a**), indicating that the Si wafer substrate was exposed. **Figures 4e** and **4f**, which show high-resolution Ir *4f* spectra, demonstrate the chemical evolution of hexachloroiridate (Ir $4f_{7/2}$: 61.18 eV, splitting: 2.97 eV) infiltrated BCP thin films into $Ir^{(III)}$ (Ir $4f_{7/2}$: 63.84 eV, splitting: 3.11 eV) and $Ir^{(IV)}$ (Ir $4f_{7/2}$: 62.29 eV, splitting: 3.08 eV) oxide (corresponding survey spectra are in **Figure S7b**). Overall, the XPS spectra given in **Figure 4** substantiate the formation of PGM/PGM oxide nanostructures from the BCP templating approach.

After substantiating the structure and composition of nanostructured PGM thin films from BCP templates, the next set of experiments examined electrochemical activity as a function of morphology and periodic feature size of the nanostructured Pt. Reactivity was assessed with arguably the most basic electrochemical reaction in acidic environments – HER/HOR (i.e., a hydrogen pump). As discussed earlier, Interdigitated electrode (IDE) chips were selected for electrochemical activity assessments because they are compatible with the BCP templating process. A drawback of IDEs is that they do not contain a reference electrode, which is useful for determining polarization contributions corresponding to individual half-reactions. Despite this drawback, IDEs are a valuable electrochemical testing platform because they are amenable to electrochemical experiments with thin film polymer electrolytes. Conventional electrocatalyst evaluations with reference electrodes are traditionally performed with rotating disk electrode (RDE) setups or h-cell setups that require liquid supporting electrolytes. It is worth noting that electrocatalytic activity can be drastically different between liquid electrolytes and polymer electrolytes[40] and working with liquids limits the temperature range for assessing electrocatalytic activity. LT-PEMFCs[5], commercial electrochemical hydrogen pumps[41], and gas-phase electrolyzers (carbon dioxide[42] and water[43]) do not use liquid supporting electrolytes; hence, it is important to study electrochemical reactivity with thin film polymer electrolytes that are often used as electrode binders. Another conventional approach for electrocatalyst evaluation is the use

of membrane electrode assemblies (MEAs)[44], but this platform does not usually contain a reference electrode (unless HER or HOR occurs at one of the electrodes with large platinum loadings in acidic media) and is costly due to: i.) the use of bulk ion-exchange membranes, ii.) the need for MEA hardware, and iii.) the time required for fabricating and breaking-in MEAs. Furthermore, MEAs are not good platforms for probing how thin film electrocatalysts influence electrochemical reactivity. Overall, IDE chips are effective high-throughput experimental platform for investigating how the geometry of nanostructured electrocatalysts, and various thin film polymer electrolytes, influence electrochemical reactions.

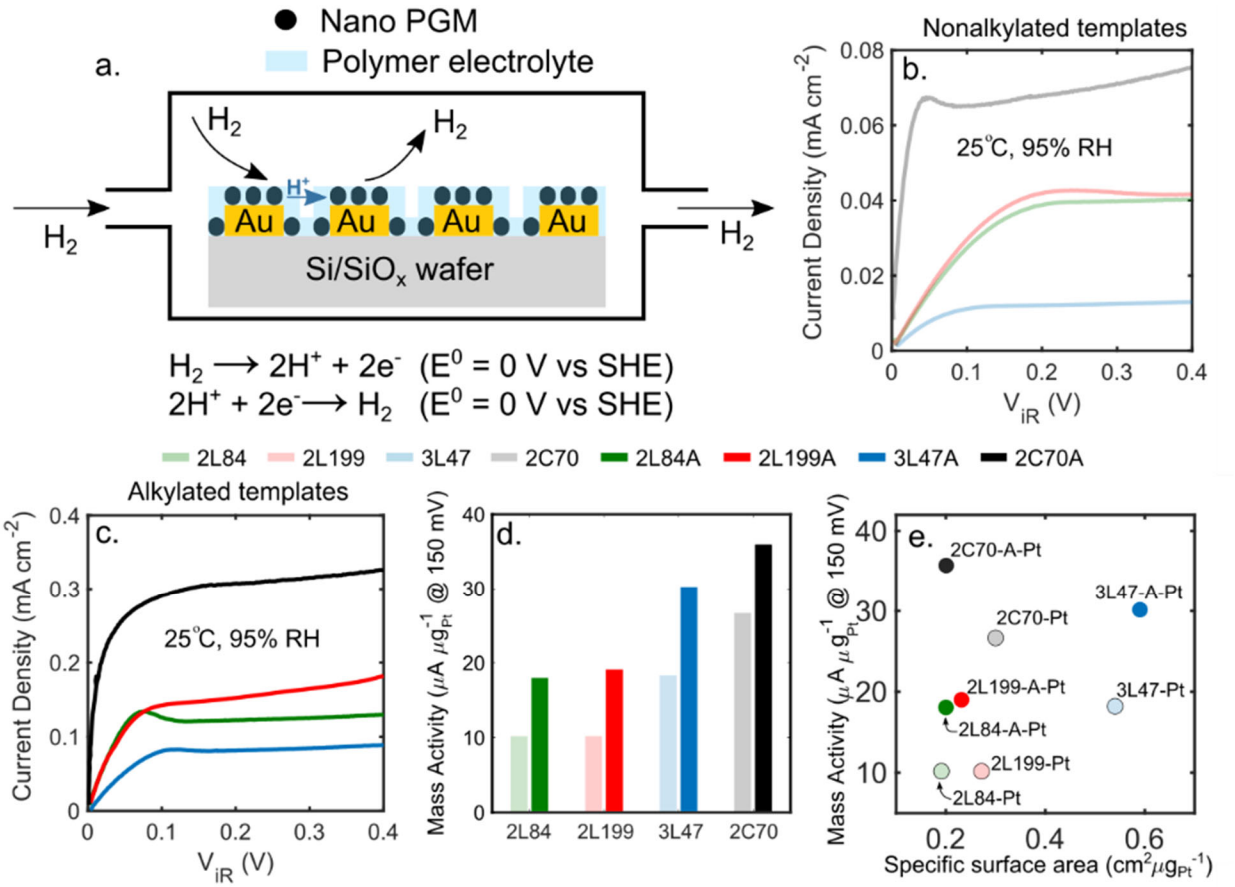


**Figure 5.** a.) Hydrogen pump setup for an Au-IDE with nanoscale Pt catalyst. This image provides the half-cell reactions for HER/HOR. b.) iR-corrected voltammograms for the hydrogen pump for nanoscale Pt of different morphologies prepared from non-alkylated BCP templates. c.) iR-corrected voltammograms for the hydrogen pump for nanoscale Pt of different morphologies prepared from alkylated BCP templates. d.) Mass activity values at 150 mV for the Pt nanostructures from both alkylated and non-alkylated templates. The solid bars correspond to nanostructures from alkylated BCP templates while the faded bars represent nanostructures from non-alkylated BCP templates (e) Mass activity vs surface area of Pt nanostructures per Pt mass loading. The solid dots refer to nanostructures

from alkylated BCP templates and non-filled dots correspond to nanostructures from non-alkylated BCP templates.

**Figure S8** shows the electron micrograph of metallic nanostructures from the BCP templating process at the interface of the electrode and silicon oxide surfaces on the IDE. The metallic nanostructures developed on Si wafers (seen in **Figure 2**) were also observed uniformly across the IDE. The nanowire structures prepared from self-assembled lamellae samples do not short the IDE as the lamellae cannot form interconnected, continuous pathways over 100 μm channel widths[21].

**Figure 5a** depicts the hydrogen pump process on the Au current collector IDEs (referred to hereafter as Au-IDEs) containing nanoscale electrocatalysts and a thin film of Nafion® polymer electrolyte. **Figure S9** shows pictures of the experimental setup for hydrogen pump experiments. Prior to starting the hydrogen pump experiments, the following control experiments were performed: i.) LSV with an Au-IDE with nanoscale Pt electrocatalyst in a chamber with humidified nitrogen and no hydrogen (**Figure S10a**), and ii.) LSV with an Au-IDE containing no Pt electrocatalysts (i.e. bare Au-IDE) with humidified hydrogen (**Figure S10b**). The first control experiment revealed that Au-IDEs with nanoscale Pt catalysts do not show current responses > 0.002 mA $cm^{-2}$ in the voltage range of 0 to 0.4 V with a humidified nitrogen. The second control experiment established that bare IDEs with Au current collectors are not significantly active for HER/HOR (i.e., current response < 0.003 mA $cm^{-2}$).

After completing control experiments, the hydrogen pump was assessed on Au-IDE chips featuring different nanoscale Pt geometries and Nafion® polymer electrolyte at 25 °C under hydrogen at 95% relative humidity. **Figures 5b** and **5c** plot the current density versus iR-corrected voltage ($V_{iR}$) from LSV experiments with Pt nanostructures from non-alkylated and alkylated templates, respectively. The Pt nanostructures templated from the PS*b*PVP/$NMP^+$ consistently gave larger current responses than Pt nanostructures templated from PS*b*PVP. The cylinder forming nanostructures (2C70)

from PS*b*PVP/NMP$^+$ showed the largest current density response while 3L47 from PS*b*PVP had the lowest current response for HER/HOR.

**Figure 5d** plots the mass activity values (μA $\mu g_{Pt}^{-1}$) of the nanostructured PGM electrocatalysts prepared from various self-assembled BCP templates at 150 mV (the procedure for calculation of mass activities is in Figure S5b). **Figure 5e** plots the same mass activity values versus PGM surface area per unit PGM loading (reported in **Table 2**). Similar to the observations in **Figures 5b** and **5c**, **Figures 5d and 5e** show that the mass activity values from alkylated BCP templates were 35 to 94% greater than non-alkylated BCPs. However, the increase in mass activity did not arrive from greater surface area of the Pt nanostructure when normalized to PGM loading because the Pt nanostructures from alkylated BCP templates had greater mass activity with about the same or less surface area per Pt loading.

The Pt nanowire samples from lamellae forming BCPs in **Figure 5e** showed an almost 2x increase in mass activity when the PGM surface area per PGM loading increased about 3x (i.e., from 0.19 $cm^2$ $\mu g_{Pt}^{-1}$ to 0.59 $cm^2$ $\mu g_{Pt}^{-1}$). This increase in mass normalized surface area hailed from the selection of the 3L47 BCP template that give periodic feature sizes of 22 nm that yields Pt nanowire diameters of 11 nm. It is worth noting that 8.5 nm wire diameters are possible with PS*b*PVP[45] if the degree of polymerization is reduced further. Taller nanostructures may also be achieved by starting with thicker self-assembled BCP films[46]. Interestingly, differences in mass activity values for 2L84 and 2L199 were not that different, but this can be accounted for by the height differences between these samples resulting in a similar PGM surface area per PGM loading. In other words, the smaller feature sizes of 2L84 were off-set by its shorter structures when compared to 2L199 – which had bigger feature sizes.

With respect to the nanoscale Pt cylinders from PS*b*P4VP/NMP$^+$, the standing cylinder nanostructures had the largest mass activity despite not having the largest PGM surface area value per PGM loading. This observation first illustrates that mesoscale control of the nanostructure is important

for improved current responses and may be ascribed to the better mass transfer of hydrogen gas into the standing cylinder morphology.

It is important to note that the HER/HOR mass activity values in **Figure 5** are fairly small when compared to hydrogen pumps based upon membrane electrode assemblies (MEAs) with Nafion® as a polymer electrolyte membrane separator and electrodes featuring Pt nanoparticle on high surface area carbon. For example, Gasteiger and co-workers[47] showed exchange current density values ($i_{0,m}$) on a mass basis of 5 x $10^5$ A $g_{Pt}^{-1}$ at 80 °C where the mass activity values with 150 mV overpotential in this work is in the only reached 3.5x$10^1$ A $g_{Pt}^{-1}$ at 25 °C. The almost 4 orders of magnitude lower mass activities were ascribed to the different experimental setup as well as the lower temperature. Another potential reason for the low activity for HER/HOR with nanoscale Pt on IDEs from self-assembled BCP templates could hail from the choice of chloroplatinate precursor because the presence of chloride hampers reactivity[48]. Additionally, it is unclear how mass transfer in these thin film nanostructures and across thin film polymer electrolytes affect mass activity values. These considerations will be examined in future work. Nevertheless, the low mass activity values did not hinder us from drawing conclusions as to how the nanostructure of Pt influenced electrochemical HER/HOR reactivity.

The fabrication scheme to prepare dense PGM electrocatalysts on IDE chips is versatile for studying other electrochemical reactions, such as water electrolysis, and with different electrolytes. Prior to working with polymer electrolytes, water electrolysis was examined on Pt current collector IDEs (referred to hereafter as Pt-IDEs) with and without nanoscale electrocatalysts with 0.1 M perchloric acid ($HClO_4$). The metal of the current collector on the IDE was switched because of Au's reactivity with $HClO_4$ under applied potentials. Furthermore, to catalyze the more challenging water reduction (i.e. oxygen evolution reaction), the nanoscale catalyst used was 11 nm $IrO_x$ nanowires from 3L47-A BCP templates, while the Pt current collector catalyzed the more facile hydrogen evolution reaction. $HClO_4$ was selected over other acids (e.g., sulfuric, phosphoric, and hydrochloric) because the

perchlorate anion has the least interference with PGM electrocatalysts. As seen in **Figures 6a – c**, the IDE with 11 nm $IrO_x$ nanowires were substantially more reactive for water electrolysis over a bare Pt-

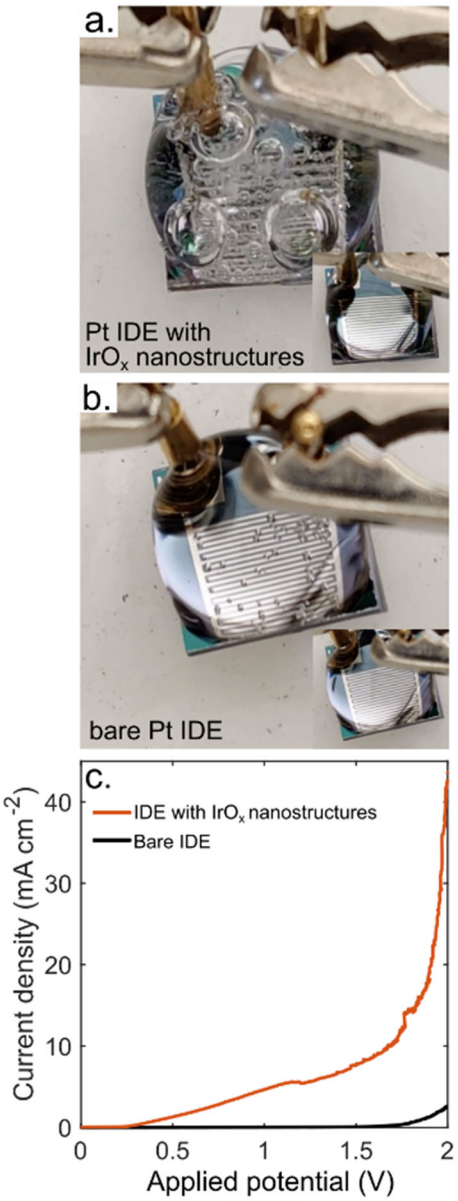


**Figure 6.** Photographs of water electrolysis in 0.1 M $HClO_4$ at 2 V and 25 °C on a.) Pt-IDE with 11 nm $IrO_x$ nanowires and b.) Pt-IDE with no nanoscale electrocatalyst. Inset images are the IDE chips at 0 V. c.) LSV from the water electrolysis experiments with the Pt-IDE with and without $IrO_x$ NW electrocatalyst in 0.1 M $HClO_4$ and 25 °C.

IDE. The photographs in **Figures 6a** and **6b** depict water splitting activity observed on Pt-IDE chips with a drop of 0.1 M perchloric acid at 2 V. The inset images in the photographs, which show the same experimental setup at 0 V, convey the IDEs to be identical as the nanostructured catalyst layer is

invisible to the naked eye. **Figure 6c** shows that the $IrO_x$ nanowires on the Pt-IDE had 9x more current density at 2 V when compared to the bare Pt-IDE. A video of the electrolysis during LSV scans up to 2V is provided in the SI. **Figures 6a – c** demonstrate that the IDE platform is flexible for water electrolysis studies with liquid supporting electrolytes.

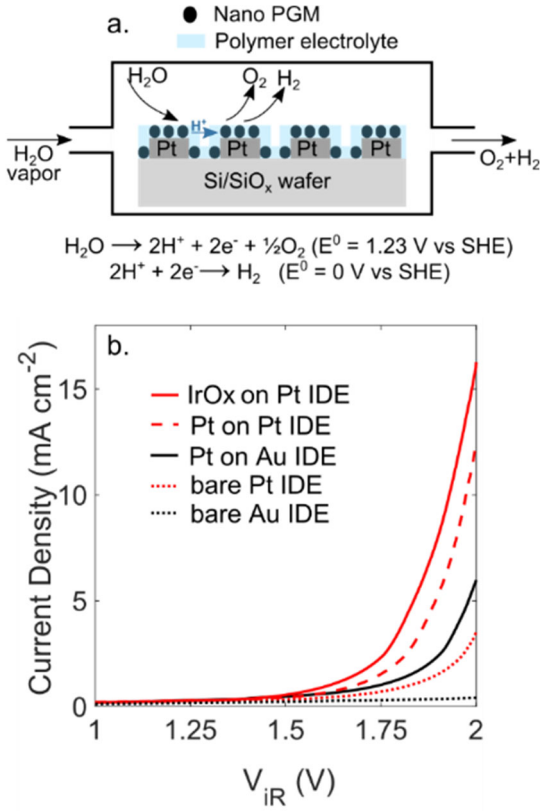


**Figure 7.** a.) Water electrolysis setup using water vapor and Pt- or Au-IDE chips with or without nanoscale PGM electrocatalysts with thin film Nafion® as electrolyte. b.) LSV curves for electrolysis of water vapor (95% RH) at 25 °C with various IDE chip configurations.

In the next set of experiments, water electrolysis was performed with water vapor (i.e., 95% humidified nitrogen) and with a thin film Nafion® polymer electrolyte instead of 0.1 M $HClO_4$. The setup with water vapor and a thin film (8 to 12 nm) polymer electrolyte is illustrated in **Figure 7a**. Because the corrosive liquid acid was removed, these experiments examined water electrolysis with both Au- and Pt-IDEs with and without Pt and $IrO_x$ electrocatalysts generated from the alkylated 3L47 template. **Figure 7b** shows LSV curves taken under nitrogen at 95% humidity with Nafion® as the electrolyte with various types of IDEs. The Pt-IDEs with nanostructured Pt electrocatalysts show higher electrocatalytic activity than bare Pt-IDEs. It is worth noting that the Pt in the current collectors on the

IDE, which is about 150 nm thick, has significantly more Pt than the Pt in the nanowires from self-assembled BCPs. Hence, the nanostructured Pt is able to significantly augment water electrolysis through its higher surfaces and greater Pt utilization. The Pt-IDEs decorated with $IrO_x$ nanowires provided the highest activity among the samples considered because the Pt current collector is effective for promoting the facile HER and the high surface area $IrO_x$ facilitates the sluggish OER. As previously stated, the IDEs do not have a reference electrode and hence one cannot delineate the overpotential contributions from each half-cell reaction. However, the HER overpotential in acid is marginal compared to OER; and the bulk of overpotential in iR-corrected polarization curves above the on-set potential hail from OER. Hence, the IDE platform is a versatile setup for examining how different electrolytes and electrocatalysts influence water electrolysis and the challenging OER.

## 3. Conclusion

A series of PGM nanostructures of varying geometric features were fabricated with self-assembled PS*b*PVP block copolymers as templates and tested for electrochemical activity on IDE chips with model reactions – HER/HOR in a hydrogen pump and HER/OER in water electrolysis. It is shown that adopting an ion containing BCP electrolyte as the template over a non-ionic variant (i.e., PS*b*PVP/$NMP^+$ versus PS*b*PVP) yields greater PGM loadings per geometric area and 34 to 95% improvement in mass activity in hydrogen pump experiments. For the three lamellar geometries considered, mass activity in the hydrogen pump was enhanced by about a factor of two when increasing the surface area per PGM loading by about 3x. The mass activity values in hydrogen pump experiments for cylindrical platinum nanostructures were more active than platinum nanowire nanostructures, but the origins of this greater activity are currently unknown and are not attributed to greater surface area per loading. Additionally, the nanostructured PGM on IDE chips were effective for water electrolysis and could discriminate activity differences between different PGM types (e.g., $IrO_x$ versus Pt). Overall, IDE chips with electrocatalysts from self-assembled BCPs represent a promising platform for i.) high throughput studies that compare and probe the intrinsic activity of electrocatalysts

as a function of nanostructure geometry and composition and ii.) investigating how thin film ionomer-electrocatalyst interfaces govern electrochemical behavior.

## 4. Experimental Section

*Materials.* All block copolymers (BCPs) were purchased from Polymer Source, Inc. and used as is. IDEs with Pt current collectors were obtained from Electronics Design Center, Case Western Reserve University. IDEs with Au current collectors were prepared in the LSU Nanofabrication facility using optical lithography following the procedure of Arges *et al.*[49] Both types of IDEs consisted of 22 electrode teeth, each of which were 0.45 cm long, 0.1mm wide, and 150 nm thick. The spacing between each electrode was 0.1 mm. The following materials and chemicals were used in the study: silicon wafers with native oxide coating (Pure wafer Inc., arsenic doped, 1 – 5 mΩ-cm), $Si/SiO_x$ wafers (WRS materials, 1 μm thick thermally grown oxide layer), perchloric acid (EMD Millipore, 70% OmniTrace™ Ultra grade), Nafion® solution (Fuel Cell Store, 20% (w/w) in 1-propanol, D2020), photoresist (S1813, Microchem Lab.), titanium and gold pellets for thermal evaporation (99.999%, ACI Alloys, Inc.), ultrapure grade nitrogen and hydrogen gases (Airgas). Hydrogen peroxide, iodomethane, chloroplatinic acid, potassium hexachloroiridate, acetone, toluene, tetrahydrofuran, and hydrochloric acid, nitric acid, sulfuric acid, and Pt and Ir standards for ICP-OES were purchased from Sigma Aldrich, Fischer Scientific, or VWR and used as is. Deionized (DI) water (18.2 MΩ, < 10 ppb TOC) used in this work was generated with 2 hours of use using a MilliQ from Millipore.

*Random copolymer synthesis and preparation of non-preferential layers.* **Scheme S1** and **Tables S1** and **S2** detail the synthetic procedure[49] (nitroxide mediated radical polymerization), molecular weights and polydispersity indices (PDI) for poly(styrene-*rand*-2-vinyl pyridine) (PS*r*P2VP-OH). **Figure S11a** provides a representative size exclusion chromatography (SEC) trace of PS*r*P2VP-OH and **Figure S11b** gives the $^1$H NMR of a representative PS*r*P2VP-OH. A 1% (w/w) toluene solution of PS*r*P2VP-OH random copolymer was spincoated onto the substrate (IDE or Si wafer) surface and grafted under $N_2$ at 200 °C for 10 min. Thereafter, any excess, non-grafted brush was removed from the substrate by

repeated sonications in toluene, leaving behind a non-preferential surface. The surface modification was confirmed via Tensiometry (Figure SI2).

*Block copolymer self-assembly.* The procedure for preparing perpendicular lamellae from self-assembled PS*b*P2VP was adopted from Arges *et al.*[39] This procedure commences with spin coating the BCPs in solution onto substrates with non-preferential surfaces. After spin coating, the BCP thin films are solvent annealed with acetone vapor in a flow chamber[39, 50]. The annealing method fosters microphase separation and also provides a non-preferential layer at the free surface for perpendicular orientation of the BCP thin films. The self-assembly of the cylinder-forming BCP (2C70) follows a slightly different procedure[51]. Here, the 2C70 BCP toluene solution (1% (w/w)**)** was spin-coated directly onto substrates with no random copolymer brush and solvent vapor annealed with THF in a flow chamber to generate self-assembled perpendicular cylinders.

*Alkylation and Incipient Wetness Impregnation.* The pyridine moiety in PS*b*PVP was alkylated to yield N-methyl pyridinium iodide through a Menshutkin reaction by sealing the sample substrates in 150 ml jars alongside opened vials of iodomethane (0.7 mL of liquid in a 1 mL vial) [39] . The substrates were exposed to iodomethane for 4 hours. Both alkylated and non-alkylated samples of self-assembled PS*b*PVP were immersed in either 10 mM $H_2PtCl_6$ (in water) or 10 mM $K_2IrCl_6$ (in 0.9% HCl) for 3 hours. During this process, the iodide anions in the alkylated PS*b*PVP (termed PS*b*PVP/$NMP^+$) were ion-exchanged with chlorometallates ($[MCl_6]^{2-}$) ($M \in [Pt, Ir]$). The non-alkylated pyridine groups in PS*b*PVP/$NMP^+$ were also partially protonated for further $[MCl_6]^{2-}$ uptake. The non-alkylated PS*b*PVP samples only had $[MCl_6]^{2-}$ uptake through protonation of the nitrogen in the pyridine moiety.

*Plasma treatment*. The metal salt impregnated BCP films were then subjected to a sequence of dry treatment steps in an Oxford PlasmaLab System 100 RIE tool. Oxygen plasma treatment was carried

out at 50 W RF power, 70 mTorr chamber pressure, and 50 sccm gas flow rate for 7.5 min. This step removed most organic matter and converted the $[MCl_6]^{2-}$ to its oxide form ($M_xO_y$). Subsequently, argon plasma treatment was carried out on the $PtO_x$ samples at 50 W RF power, 90 mTorr chamber pressure, and 50 sccm gas flow rate for 15 s in order to reduce the $PtO_x$ to elemental Pt. No argon treatment was performed on the $IrO_x$ samples.

*Electrochemical testing*. The nanostructured PGMs from BCPs were prepared on IDE platforms for assessing electrochemical activity. After nanostructure PGM formation on IDEs, a 0.5 %(w/w) solution of Nafion® polymer electrolyte was spincoated on the sample and air dried to yield 8 to 12 nm thick films. Ellipsometry was used for film thickness measurements (note: the substrates containing the spincoated Nafion® polymer electrolyte were bare silicon wafer substrates and not the IDEs with nanostructured Pt as the topographical electrodes interfere with ellipsometry). Prior to electrochemical experiments, the electrolyte and nanostructured electrocatalyst layer were removed from the electrode pads of the IDEs with a cotton swab to ensure proper electrical contact. The sample to be tested was sealed inside a custom-built stainless-steel chamber equipped with a PTFE sample mount, gas inlets and outlets, electrical contacts, and a temperature probe. All experiments were carried out at 95% to 99% RH at ambient temperature (25 – 28 °C) with a gas flow rate of 0.1 SLPM. Relative humidity was controlled through manipulation of the bubbler temperature and cell temperature. **Figure S9** provides photographs of the test chamber setup.

After loading the IDE into the chamber and sealing, the appropriate humidified carrier gas was passed across the sample for at least 1 h to allow the Nafion® polymer electrolyte to absorb water, equilibrate, and reach a steady electrolyte resistance value[52]. Linear sweep voltammetry (LSV) experiments were conducted between 0 and 0.4 V for hydrogen pump (i.e., HER/HOR), and between 0 and 2 V for water electrolysis (HER/OER). All measurements were made using a Gamry Potentiostat (3000AE) with a scan rate of 20 mV $s^{-1}$. Potentiostatic Electrochemical Impedance Spectroscopy (EIS) experiments were conducted between $10^5$ – 0.1 Hz with an amplitude of 10 mV and a bias potential of 400 mV. The

electrolyte resistance ($R_\Omega$) calculated from EIS was used to generate iR-corrected LSV curves ($E_{iR} = E - i \cdot R_\Omega$).

*Digestion and ICP-OES.* The nanostructured Pt and $IrO_x$ prepared from different BCP templates on 1 $cm^2$ Si wafers were immersed in 10 ml of aqua regia (mixture of 7.5 ml of 37% HCl and 2.5 ml of 69% $HNO_3$) and dissolved completely using a microwave digestion apparatus[53]. The resultant solutions were diluted to a final volume of 25 ml and assayed using a Perkin Elmer Optima 8x00 Inductively Coupled Plasma – Optical Emission Spectrometer (ICP-OES) calibrated with Pt and Ir references. Four counts of each nanostructure sample were studied and averaged.

*Electron and Atomic Force Microscopy.* The BCPs and Pt nanostructures were observed under a Field Emission Scanning Electron Microscope (Quanta™ 3D DualBeam™ FEG FIB/SEM) using an operating voltage of 5 to 10 kV and a spot size of 3.5 – 4 nm while maintaining a working distance of 2 to 3 mm. AC mode Atomic Force Microscopy was performed using a Horiba SmartSPM™ 1000 at the LSU Nanofabrication Facility using uncoated Si cantilevers (ACTA-SS, k = 37 N/m, 125 μm length) operating at a resonant frequency of 287 kHz at a free amplitude of ~30 nm.

*Ellipsometry and Tensiometry.* Thickness of the block copolymer thin films (and of the underlying polymer brushes) were determined using a J.A. Woollam Co., Inc. Ellipsometer (Model RC2). An Attension Theta optical tensiometer from Biolin Scientific was used to measure water contact angle values.

*X-ray Photoelectron Spectroscopy.* XPS was performed at the LSU Center for Advanced Microstructures and Devices (CAMD) using an Omicron EA 125 hemispherical electron analyzer with a five-channel detector and a DAR-400 dual Mg/Al X-ray source resided on the main chamber at the 5m-TGM beamline. The main chamber was maintained at a base pressure of $10^{-10}$ Torr. The XPS spectra were collected with a pass energy of 25 eV and a source power of 150 W (15 kV and 10 mA). The energy calibration of all spectra was done using the C*1s* spectral line (284.8 eV).

*Grazing Incidence Small Angle X-ray Scattering.* GISAXS was conducted on the metal nanostructures on Si wafer at the Advanced Photon Source (beamline 8-ID-E)[54], Argonne National Laboratory. All experiments were performed using a 100 μm × 20 μm (H x V) beam of 10.91 keV X-rays incident on the sample at an angle of 0.14° (footprint: 0.82 $mm^2$), and 0.17° (footprint: 0.68 $mm^2$),with the 2D scattering pattern collected by a Pilatus 1M detector (pixel size 0.172 mm × 0.172 mm) held at a distance of 2185 mm from the sample. Profiles along the in-plane scattering vector were obtained by integrating over all values of the out-of-plane scattering vector ($q_z$) in the full region exhibiting peaks in the Yoneda bands, to obtain the scattering intensity as a function of the photon momentum transfer in the plane of the sample, I($q_y$), using the GIXSGUI package for MATLAB[55]. Domain spacing ($L_0$) was calculated from peak positions ($q_y$) obtained for both 0.14° and 0.17° as $L_0 = 2\pi/q_y$ and averaged.

## Supporting Information

Supporting Information is available from the Wiley Online Library or from the author.


## Acknowledgements

This material is based upon work supported by the U.S. Department of Energy, Office of Science, Office of Basic Energy Sciences Separation Science program under Award Number DE-SC0018989. This research used resources of the Advanced Photon Source, a U.S. Department of Energy (DOE) Office of Science User Facility operated for the DOE Office of Science by Argonne National Laboratory under Contract No. DE-AC02-06CH11357 (Beamline 8-ID-E for GI-SAXS experiments). LSU Shared Instrumentation Facilities, Nanofabrication Facility and Center for Advanced Microstructures and Devices (CAMD) were used for this work. DB, SK, and CGA acknowledge Professor Kevin McPeak's help with cleanroom operation. DB and CGA acknowledge Professor Bhuvnesh Bharti's assistance with Tensiometry.


## Conflict of Interest

The authors declare no conflict of interest


Received: (( ))
Revised: (( ))
Published online: (( ))


## References


[1] X. Ren, Q. Lv, L. Liu, B. Liu, Y. Wang, A. Liu, G. Wu, *Sustainable Energy Fuels* **2020,** *4* (1), 15-30.
[2] J. Lai, R. Luque, G. Xu, *ChemCatChem* **2015,** *7* (20), 3206-3228.
[3] L. Wang, A. Holewinski, C. Wang, *ACS Catal.* **2018,** *8* (10), 9388-9398.
[4] M. K. Debe, *Nature (London, U. K. )* **2012,** *486* (7401), 43-51.
[5] A. Kongkanand, M. F. Mathias, *J. Phys. Chem. Lett.* **2016,** *7* (7), 1127-1137.
[6] Y. Gu, J. St-Pierre, H. J. Ploehn, *Langmuir* **2008,** *24* (21), 12680-12689.

[7] J. M. Elliott, G. S. Attard, P. N. Bartlett, N. R. B. Coleman, D. A. S. Merckel, J. R. Owen, *Chem. Mater.* **1999,** *11* (12), 3602-3609.
[8] J. Chai, D. Wang, X. Fan, J. M. Buriak, *Nat. Nanotechnol.* **2007,** *2* (8), 500-6.
[9] K. Brassat, D. Kool, J. Bürger, J. K. N. Lindner, *Nanoscale* **2018,** *10* (21), 10005-10017.
[10] N. Markovic, H. Gasteiger, P. N. Ross, *J. Electrochem. Soc.* **1997,** *144* (5), 1591-1597.
[11] S. Ji, L. Wan, C. -C. Liu, P. F. Nealey, *Prog. Polym. Sci.* **2016,** *54-55*, 76-127.
[12] Y. Kambe, C. G. Arges, S. N. Patel, M. P. Stoykovich, P. F. Nealey, *Electrochem. Soc. Interface* **2017,** *26* (1), 61-67.
[13] Y. Kambe, C. G. Arges, D. A. Czaplewski, M. Dolejsi, S. Krishnan, M. P. Stoykovich, J. J. de Pablo, P. F. Nealey, *Nano Lett.* **2019,** *19* (7), 4684-4691.
[14] C. Sinturel, F. S. Bates, M. A. Hillmyer, *ACS Macro Lett.* **2015,** *4* (9), 1044-1050.
[15] H. Hu, M. Gopinadhan, C. O. Osuji, *Soft Matter* **2014,** *10* (22), 3867-89.
[16] L. Leibler, *Macromolecules* **1980,** *13* (6), 1602-17.
[17] F. S. Bates, G. H. Fredrickson, *Annu. Rev. Phys. Chem.* **1990,** *41*, 525-57.
[18] K. W. Guarini, C. T. Black, K. R. Milkove, R. L. Sandstrom, *J. Vac. Sci. Technol. , B: Microelectron. Nanometer Struct. --Process. , Meas. , Phenom.* **2001,** *19* (6), 2784-2788.
[19] A. J. Hong, C. -C. Liu, Y. Wang, J. Kim, F. Xiu, S. Ji, J. Zou, P. F. Nealey, K. L. Wang, *Nano Lett.* **2010,** *10* (1), 224-229.
[20] R. Ruiz, H. Kang, F. A. Detcheverry, E. Dobisz, D. S. Kercher, T. R. Albrecht, J. J. de Pablo, P. F. Nealey, *Science* **2008,** *321* (5891), 936-9.
[21] K. M. Diederichsen, R. R. Brow, M. P. Stoykovich, *ACS Nano* **2015,** *9* (3), 2465-2476.
[22] K. Shin, K. A. Leach, J. T. Goldbach, D. H. Kim, J. Y. Jho, M. Tuominen, C. J. Hawker, T. P. Russell, *Nano Lett.* **2002,** *2* (9), 933-936.
[23] W. Lei, R. Ricardo, H. G. He, C. P. Kanaiyalal, L. Jeffery, Z. Gabriel, A. D. Elizabeth, B. Alexei, R. A. Thomas, F. N. Paul, *J. Micro/Nanolithogr. , MEMS, MOEMS* **2012,** *11* (3), 1-6.
[24] Y. S. Jung, J. H. Lee, J. Y. Lee, C. A. Ross, *Nano Lett.* **2010,** *10* (9), 3722-3726.
[25] S. H. Joo, S. J. Choi, I. Oh, J. Kwak, Z. Liu, O. Terasaki, R. Ryoo, *Nature (London, U. K. )* **2001,** *412* (6843), 169-172.
[26] K. H. Tu, W. Bai, G. Liontos, K. Ntetsikas, A. Avgeropoulos, C. A. Ross, *Nanotechnology* **2015,** *26* (37), 375301.
[27] K. Mikkelsen, B. Cassidy, N. Hofstetter, L. Bergquist, A. Taylor, D. A. Rider, *Chem. Mater.* **2014,** *26* (24), 6928-6940.
[28] A. K. Taylor, D. S. Perez, X. Zhang, B. K. Pilapil, M. H. Engelhard, B. D. Gates, D. A. Rider, *J. Mater. Chem. A* **2017,** *5* (40), 21514-21527.
[29] C. -F. Cheng, H. -Y. Hsueh, C. -H. Lai, C. -J. Pan, B. -J. Hwang, C. -C. Hu, R. -M. Ho, *NPG Asia Materials* **2015,** *7* (4), e170-e170.
[30] J. Lee, A. K. Mishra, C. Choi, D. Kim, E. Y. Kim, K. Yong, J. K. Kim, *ACS Appl. Mater. Interfaces* **2020,** *12* (13), 15667-15674.
[31] Y. Choi, S. K. Cha, H. Ha, S. Lee, H. K. Seo, J. Y. Lee, H. Y. Kim, S. O. Kim, W. Jung, *Nat. Nanotechnol.* **2019,** *14* (3), 245-251.
[32] S. K. Cha, J. H. Mun, T. Chang, S. Y. Kim, J. Y. Kim, H. M. Jin, J. Y. Lee, J. Shin, K. H. Kim, S. O. Kim, *ACS Nano* **2015,** *9* (5), 5536-5543.
[33] S. K. Cha, G. Y. Lee, J. H. Mun, H. M. Jin, C. Y. Moon, J. S. Kim, K. H. Kim, S. -J. Jeong, S. O. Kim, *ACS Appl. Mater. Interfaces* **2017,** *9* (18), 15727-15732.
[34] W. Lee, S. Lee, A. S. Tang, C. Kim, R. Liu, K. Im, H. -T. Jung, C. A. Ross, *ACS Appl. Nano Mater.* **2020**.
[35] C. Cummins, A. Gangnaik, R. A. Kelly, D. Borah, J. O'Connell, N. Petkov, Y. M. Georgiev, J. D. Holmes, M. A. Morris, *Nanoscale* **2015,** *7* (15), 6712-6721.
[36] A. Selkirk, N. Prochukhan, R. Lundy, C. Cummins, R. Gatensby, R. Kilbride, A. Parnell, J. Baez Vasquez, M. Morris, P. Mokarian-Tabari, *Macromolecules* **2021,** *54* (3), 1203-1215.
[37] Y. Gan, Z. -d. Wang, Y. Shi, C. -q. Guo, H. -y. Tan, Z. -x. Lu, C. -f. Yan, *Electrochim. Acta* **2018,** *283*, 1-10.

[38] Y. Gan, Z. -d. Wang, Y. Shi, C. -q. Guo, H. -y. Tan, C. -f. Yan, *Journal of Materials Science* **2018,** *53* (6), 4089-4102.
[39] C. G. Arges, Y. Kambe, H. S. Suh, L. E. Ocola, P. F. Nealey, *Chem. Mater.* **2016,** *28* (5), 1377-1389.
[40] C. M. Zalitis, D. Kramer, A. R. Kucernak, *Phys. Chem. Chem Phys.* **2013,** *15* (12), 4329-4340.
[41] C. Jackson, L. F. J. M. Raymakers, M. J. J. Mulder, A. R. J. Kucernak, *J. Power Sources* **2020,** *472*, 228476.
[42] R. B. Kutz, Q. Chen, H. Yang, S. D. Sajjad, Z. Liu, I. R. Masel, *Energy Technol. (Weinheim, Ger. )* **2017,** *5* (6), 929-936.
[43] J. C. Fornaciari, M. R. Gerhardt, J. Zhou, Y. N. Regmi, N. Danilovic, A. T. Bell, A. Z. Weber, *J. Electrochem. Soc.* **2020,** *167* (10), 104508.
[44] H. A. Gasteiger, S. S. Kocha, B. Sompalli, F. T. Wagner, *Appl. Catal. B* **2005,** *56* (1), 9-35.
[45] S. Xiong, D. Li, S. -M. Hur, G. S. W. Craig, C. G. Arges, X. -P. Qu, P. F. Nealey, *Macromolecules (Washington, DC, U. S. )* **2018,** *51* (18), 7145-7151.
[46] A. M. Welander, G. S. W. Craig, Y. Tada, H. Yoshida, P. F. Nealey, *Macromolecules (Washington, DC, U. S. )* **2013,** *46* (10), 3915-3921.
[47] K. C. Neyerlin, W. Gu, J. Jorne, H. A. Gasteiger, *J. Electrochem. Soc.* **2007,** *154* (7), B631.
[48] N. Job, M. Chatenet, S. Berthon-Fabry, S. Hermans, F. Maillard, *J. Power Sources* **2013,** *240*, 294-305.
[49] C. G. Arges, Y. Kambe, M. Dolejsi, G. -P. Wu, T. Segal-Pertz, J. Ren, C. Cao, G. S. W. Craig, P. F. Nealey, *J. Mater. Chem A* **2017,** *5* (11), 5619-5629.
[50] Q. Lei, K. Li, D. Bhattacharya, J. Xiao, S. Kole, Q. Zhang, J. Strzalka, J. Lawrence, R. Kumar, C. G. Arges, *J. Mater. Chem. A* **2020,** *8* (31), 15962-15975.
[51] S. Park, J. -Y. Wang, B. Kim, J. Xu, T. P. Russell, *ACS Nano* **2008,** *2* (4), 766-772.
[52] A. Z. Weber, J. Newman, *Chem. Rev.* **2004,** *104* (10), 4679-4726.
[53] H. Lim, K. Kani, J. Henzie, T. Nagaura, A. S. Nugraha, M. Iqbal, Y. S. Ok, M. S. A. Hossain, Y. Bando, K. C. W. Wu, H. -J. Kim, A. E. Rowan, J. Na, Y. Yamauchi, *Nat. Protoc.* **2020,** *15* (9), 2980-3008.
[54] Z. Jiang, X. Li, J. Strzalka, M. Sprung, T. Sun, A. Sandy, S. Narayanan, D. Lee, J. Wang, *Journal of Synchrotron Radiat.* **2012,** *19*, 627-636.
[55] Z. Jiang, *J. Appl. Crystallogr.* **2015,** *48* (3), 917-926.